scientific reports

Check for updates

OPEN

In vivo production of fluorine-18 in a chicken egg tumor model of breast cancer for proton therapy range verification

Samuel España[1,2,3]✉, Daniel Sánchez-Parcerisa[1,2,4], Paloma Bragado[2,5], Álvaro Gutiérrez-Uzquiza[2,5], Almudena Porras[2,5], Carolina Gutiérrez-Neira[1,6], Andrea Espinosa[1,2], Víctor V. Onecha[1,2], Paula Ibáñez[1,2], Víctor Sánchez-Tembleque[1,2], José M. Udías[1,2] & Luis M. Fraile[1,2]

Range verification of clinical protontherapy systems via positron-emission tomography (PET) is not a mature technology, suffering from two major issues: insufficient signal from low-energy protons in the Bragg peak area and biological washout of PET emitters. The use of contrast agents including ^{18}O, ^{68}Zn or ^{63}Cu, isotopes with a high cross section for low-energy protons in nuclear reactions producing PET emitters, has been proposed to enhance the PET signal in the last millimeters of the proton path. However, it remains a challenge to achieve sufficient concentrations of these isotopes in the target volume. Here we investigate the possibilities of ^{18}O-enriched water (18-W), a potential contrast agent that could be incorporated in large proportions in live tissues by replacing regular water. We hypothesize that 18-W could also mitigate the problem of biological washout, as PET (^{18}F) isotopes created inside live cells would remain trapped in the form of fluoride anions (F-), allowing its signal to be detected even hours after irradiation. To test our hypothesis, we designed an experiment with two main goals: first, prove that 18-W can incorporate enough ^{18}O into a living organism to produce a detectable signal from ^{18}F after proton irradiation, and second, determine the amount of activity that remains trapped inside the cells. The experiment was performed on a chicken embryo chorioallantoic membrane tumor model of head and neck cancer. Seven eggs with visible tumors were infused with 18-W and irradiated with 8-MeV protons (range in water: 0.74 mm), equivalent to clinical protons at the end of particle range. The activity produced after irradiation was detected and quantified in a small-animal PET-CT scanner, and further studied by placing ex-vivo tumours in a gamma radiation detector. In the acquired images, specific activity of ^{18}F (originating from 18-W) could be detected in the tumour area of the alive chicken embryo up to 9 h after irradiation, which confirms that low-energy protons can indeed produce a detectable PET signal if a suitable contrast agent is employed. Moreover, dynamic PET studies in two of the eggs evidenced a minimal effect of biological washout, with 68% retained specific ^{18}F activity at 8 h after irradiation. Furthermore, ex-vivo analysis of 4 irradiated tumours showed that up to 3% of oxygen atoms in the targets were replaced by ^{18}O from infused 18-W, and evidenced an entrapment of 59% for specific activity of ^{18}F after washing, supporting our hypothesis that F- ions remain trapped within the cells. An infusion of 18-W can incorporate ^{18}O in animal tissues by replacing regular water inside cells, producing a PET signal when irradiated with low-energy protons that could be used for range verification in protontherapy. ^{18}F produced inside cells remains entrapped and suffers from minimal biological washout, allowing for a sharper localization with longer PET acquisitions. Further studies must evaluate the feasibility of this

[1]Grupo de Física Nuclear and IPARCOS, Facultad de CC. Físicas, Universidad Complutense de Madrid, CEI Moncloa, 28040 Madrid, Spain. [2]Instituto de Investigación Sanitaria del Hospital Clínico San Carlos (IdISSC), Ciudad Universitaria, Madrid, Spain. [3]Centro Nacional de Investigaciones Cardiovasculares (CNIC), Madrid, Spain. [4]Sedecal Molecular Imaging, Algete, Madrid, Spain. [5]Departamento de Bioquímica y Biología Molecular, Facultad de Farmacia, Universidad Complutense de Madrid, Madrid, Spain. [6]Centro de Microanálisis de Materiales, CMAM-UAM, Madrid, Spain. ✉email: sespana@ucm.es

technique in dosimetric conditions closer to clinical practice, in order to define potential protocols for its use in patients.

The number of proton therapy facilities to treat cancer has increased considerably in the last few years[1]. The main advantages of protons over other radiation therapy techniques are the large dose deposited at the end of their range, known as the Bragg peak, and the absence of dose distal to it. Therefore, the accuracy in positioning the distal edge of the proton beam is crucial for a correct dose delivery, i.e., ensuring a complete irradiation of the tumor and reducing the dose to organs at risk[2]. Several techniques have been proposed for in-vivo proton range verification, including the use of positron emission tomography (PET) imaging to quantify and locate the β^+ isotopes produced by the proton beam through nuclear reactions inside the patient[3,4]. In addition, the detection of prompt gammas emitted from excitations of the target nuclei has been suggested[5] for proton range verification. Both techniques have been already tested in clinical studies in patients[3,6]. Other studies suggested the measurement of the acoustic pressure waves generated by proton dose deposition using high frequency ultrasonic transducers[7] or the detection of radiation-induced changes in the constitution of human tissue which can be visible by MRI imaging[8]. However, research related to this topic is still needed to find a precise and reliable method for in vivo range verification that can be implemented clinically[9].

While protons deposit their dose mainly through electromagnetic interactions, β^+ isotopes are produced via nuclear reactions. Since β^+-emitters originated by proton-induced reactions on human tissues, mainly ^{11}C and ^{15}O, have a relatively high production threshold (17.9 MeV for $^{12}C(p,X)^{11}C$ and 14.3 MeV for $^{16}O(p,X)^{15}O$), they will not be formed in the proximity of the Bragg peak[10] limiting the applicability of PET imaging for proton beam range verification[11]. The use of ^{13}N produced from ^{16}O has been suggested as an alternative[12] due to the lower energy threshold (5.5 MeV), but its integrated cross-section at low energies may not be high enough[13], and the ^{13}N specific activity decreases at a fast pace, due to its shorter half life and affected by biological washout processes.

The use of dedicated in-beam PET detectors in the treatment room has been considered in several previous works[14,15]. Compared with offline PET, the available PET-isotopes are significantly increased and much shorter imaging times are required. Therefore, the influence of biological wash-out processes is reduced, and no repositioning of the patient is necessary. However, since imaging is done in the treatment room, this compromises the patient throughput. In addition, the integration of in-beam PET is technically challenging due to geometric constraints and the production of background radiation during irradiation. Further improvement was suggested by using in-beam time-of-flight-PET (TOF-PET) detectors[16].

Furthermore, the in-beam PET strategy provides the detection of the very short-lived positron emitters as ^{12}N ($T_{1/2} = 11$ ms)[17,18]. This option avoids the impact of biological washout, allows reducing acquisition time down to 50 ms, and facilitates the implementation of range measurement on a spot-by-spot basis. However, optimized PET systems are still required to increase counting statistics.

On the other hand, isotopes such as ^{18}O, ^{68}Zn, ^{63}Cu or ^{127}I exhibit a high proton-induced reaction cross sections and comparatively lower reaction thresholds[19]. Most of them are naturally occurring in trace amounts in natural elements and thus do not contribute to PET activation in human tissues. It has been suggested to use compounds with elements enriched in those isotopes as possible contrast media for proton PET range verification[20,21] as their use may facilitate Bragg-peak localization via PET. A high concentration of the contrast in the irradiated area is required in order to provide a detectable activity that can be used for proton range verification. For this purpose, the use of ^{18}O-enriched water (18-W) appears as an appealing approach[22,23] as it is a suitable substance that can reach very high concentrations in-vivo on human tissues[24] by direct intravenous, intra-arterial or intratumoral administration to the patient. Also, the substitution of regular water by 18-W does not require to modify the treatment plan computed from a CT image of the patient, as the energy deposition and biochemical effects in the target are not affected by the isotopic distribution of its constituent atoms. However, this must be verified experimentally as there might be small differences of the mean excitation energy of 18-W compared to regular water. Recently, we demonstrated the capability of 18-W for last-millimeter range verification in proton therapy by irradiating and performing a PET scan on a water phantom filled with jellified 18-W[13]. The activation produced from the contrast agent showed an excellent correlation with the dose distribution up to several hours after irradiation, due to the long half-life of ^{18}F.

In the present in-vivo study using 18-W as a contrast agent we hypothesize that, while cell membrane is permeable to regular water (and therefore also to 18-W), any ^{18}F ion produced inside the cell by activation of 18-W will remain trapped inside the cells for a relatively long time, minimizing the effects of biological washout[25]. In this work, we performed an in-vivo study to evaluate our previous phantom results in a more realistic environment. For this purpose, a chicken embryo chorioallantoic membrane tumor model of head and neck cancer was used[26]. Head and neck tumours are usually treated with radiotherapy[27], and for this type of cancers, proton therapy has demonstrated clinical efficacy and potential for toxicity reduction compared to photon therapy[28]. In our experiment, the tumor was grown on the chicken chorioallantoic membrane (CAM) and infused with a buffer containing 18-W, prior to irradiation with protons. The produced activity was monitored after irradiation with a gamma radiation spectrometer and with a PET/CT scanner in order to evaluate the capability of this technique for enhancing in-vivo range verification in proton therapy.

Materials and methods

Materials. 18-W containing 70% of ^{18}O was purchased from a commercial vendor (Sigma-Aldrich). A 18-W buffer was prepared by mixing 10X phosphate buffered saline (PBS 10×, lonza) and 70% 18-W at a ratio of 9:1 (v/v) obtaining a physiological buffer that was used to inoculate the tumors generated in this study.

In-vivo chicken embryo chorioallantoic membrane tumor model. Chick CAM assays were performed as previously described[29,30]. For these experiments we used tumorigenic HEp3 cells (T-HEp3) which are a head and neck squamous carcinoma cell line that was derived from a cervical lymph node metastasis of a patient with squamous cell carcinoma of the oral cavity in 1954[31]. Since them, it has always been kept in vivo using either chicken embryo or mice[32]. Our batch was kindly donated by Julio Aguirre-Ghiso (Mount Sinai School of Medicine, NY)[33]. Briefly, 2.5×10^5 T-HEp3 cells were inoculated on the chicken embryo CAM of specific pathogen-free (SPF), fertile, 10-day-old embryonated chicken eggs (Granja Santa Isabel, Spain) and tumors were grown for 7 days. On day 7, the eggs were transported to the accelerator facility, infused with 18-W and irradiated. Chicken embryos were euthanized by carbon dioxide inhalation using an anoxia chamber. All the experimental protocols were approved by the Universidad Complutense Ethics committee (Comunidad de Madrid) in compliance with the European Community Council Directive (2010/63/EU). We followed the Animal Research: Reporting In Vivo Experiments (ARRIVE) guidelines.

Irradiation facility. All the samples were irradiated at the Centre for Micro Analysis of Materials—Universidad Autónoma de Madrid (CMAM-UAM) using the high-current electrostatic 5-MV tandetron accelerator. The proton beam was extracted from the external microbeam line[34] at an energy of 8 MeV. The optic properties of the beam in the vacuum line were controlled by two slits in the X and Y directions, manually adjustable with micrometric screws, and by two focusing quadrupole magnets (rotated 90 degrees). The beam exits the vacuum line through an 8-µm-thick kapton window. A dedicated irradiation setup was built to accurately control the irradiation time and the beam position[35]. For this purpose, a remote-control shutter was placed at the beam exit and a 3-axis robotic stage was used to hold the samples and to align them with the beam.

Beam characterization and dosimetry. Prior to sample irradiation, the transversal spread of the beam for a given configuration was characterized using Gafchromic EBT3 film at successive distances from the kapton foil. Lateral spreads in the X and Y directions, namely σ_x and σ_y, were measured using a single-gaussian model for the spot. Longitudinal variation of the spreads was fit to a second-degree polynomial for each dimension. The parameters of these fits, along with the particle stopping power in water[36] were introduced in an analytical dose-calculation engine, based on a simplified version of FoCa[37]. This code[35] was used to produce suitable treatment plans for sample irradiation and to estimate the amount of absorbed dose from irradiation logs. Quality assurance of the plans was performed by comparing the expected dose with a plan-specific treatment verification film, after correcting for quenching effects[38].

Irradiation of eggs. Seven eggs (labeled E1–E3 for those analyzed in-vivo and T1–T4 for those analyzed ex-vivo) were irradiated with a proton beam at the CMAM facility using the same protocol as follows. Immediately prior to irradiation of each egg, 200 µL of 18-W buffer were applied dropwise locally to the surface of the CAM during 5 min to facilitate its absorption within the tumor (see Fig. 1). Afterwards, the egg was irradiated according to the following protocol. The eggs were situated at a distance of 5 cm measured from the shell to the beam exit window. The beam was estimated to travel through an additional gap of 2.5 cm of air (see Fig. 1) between the shell window and the tumour surface. The combined energy loss of the beam in the exit window + air gap was estimated to be equal to 0.50 MeV. Range in water of 7.50-MeV protons is estimated at 0.74 mm[36], so that any activation observed under our experimental conditions would correspond to activation at the last millimeter of the path in a clinical beam.

The egg was visually aligned with the beam using the robotic stage and a laser previously configured towards the beam irradiation spot (see Fig. 1). In order to ensure hitting the target, we delivered 9 shots of 10 s duration each (90 s in total), with a 1.2-mm separation to each other forming a 3×3 grid. Spot size on the surface of the tumour was calculated at $\sigma_x = 0.78$ mm and $\sigma_y = 0.89$ mm. With this spot configuration, dose homogeneity in a 2-mm radius around the tumor center was better than 10%. The egg opening window was surrounded by radiochromic film to verify a correct positioning of the samples by observing the darkening of the film produced by the proton halo. The average beam intensity employed for 6 of the eggs (E1–E2, T1–T4) was 6.0 ± 0.5 nA. Tumours were irradiated with a cumulative proton fluence of about $2.5 \cdot 10^{13}$ protons/cm^2, depositing a total surface dose in the tumour (calculated in a thickness of 100 µm) of $2.4 \cdot 10^5$ Gy. A lower dose was delivered to one of the eggs (E3) using a much lower beam intensity of 150 pA, leading to a deposited dose of 127 Gy. These larger-than-usual doses were selected in order to ensure a clear observation of the activation effect in the samples and measure decays for a longer period, regardless of the sensitivity of the scanner, for this proof-of-principle study.

In-vivo analysis (PET/CT). The activity produced on 3 of the irradiated eggs (E1 and E2 at high dose and E3 at lower dose) was monitored in-vivo using a SuperArgus[39] PET/CT scanner (Sedecal, Madrid, Spain). The field of view (FOV) of this scanner has a diameter of 12 cm and axial length of 10 cm, uses a pixelated phoswich detector technology combining LYSO and GSO crystals with a total thickness of 15 mm and provides a spatial resolution down to 0.8 mm FWHM. A 10-min PET scan was performed 1 h after irradiation for the egg irradiated at lower dose (E3) while a 9-h PET acquisition was started 3.5–4 h after irradiation for the eggs irradiated at higher dose (E1 and E2). Then, a CT scan was acquired. The viability of the chicken embryos was confirmed after the imaging session. The PET scan of E1 and E2 was reconstructed dividing the acquisition in 9 consecutive frames of 60 min, while the PET scan of E3 was reconstructed as a single frame of 10 min. PET images were reconstructed using the 3D-OSEM reconstruction software provided with the scanner[40] with $225 \times 225 \times 127$ voxels and a voxel size of 0.554 mm × 0.554 mm × 0.775 mm. Tumor volumes were manually segmented on fused PET/CT images using Amide (http://amide.sourceforge.net/) and decay curves were obtained separately for E1

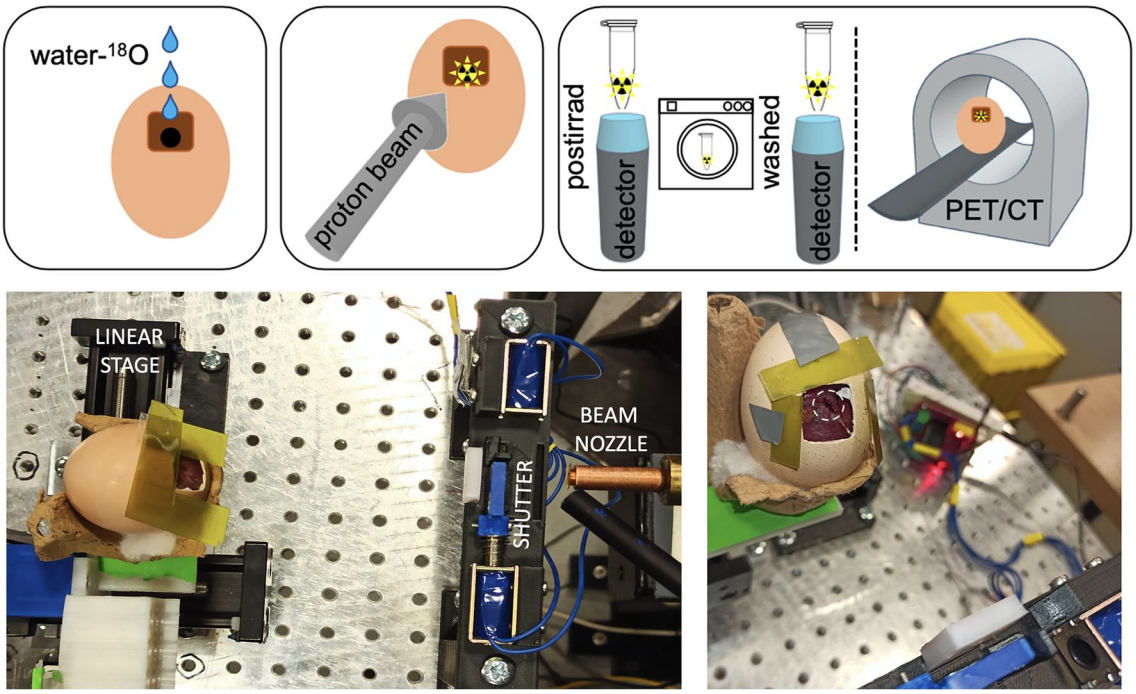

Figure 1. Top: schematic representation of the experimental protocol followed in this study. First, the eggs were inoculated with 18-W. Then, the eggs were irradiated with a proton beam of 8 MeV. Finally, 5 tumors were analyzed ex-vivo with a gamma radiation detector spectrometer and 3 eggs were analyzed on a PET/CT scanner. Bottom: pictures of the experimental setup used for the irradiation of the eggs with the external beam line at the CMAM facility. The white circle on the right picture delineates the tumor area.

Isotope	$T_{1/2}$ [min]	Reaction channel	Reaction threshold [MeV]	Integrated cross section for 7.5-MeV protons [mb MeV]
^{11}C	20.364	^{14}N(p,X)^{11}C	3.13	75.1
^{13}N	9.965	^{16}O(p,X)^{13}N	5.55	3.3
^{18}F	109.77	^{18}O(p,n)^{18}F	2.57	1130.7

Table 1. Isotopes included in the analysis of decay curves and reaction channels responsible for tumor activation (including only allowed reactions for protons of 7.5 MeV).

and E2. These curves were then fitted to an exponential following the physical decay of ^{18}F (accounting for biological washout), as all other produced isotopes have a much shorter half-life.

Ex-vivo analysis (scintillator detector). The activity produced on 4 of the irradiated eggs (T1–T4) was recorded using a gamma radiation detector composed of a $CeBr_3$ scintillation crystal with conical shape (base and top diameters of 25 and 19 mm respectively and 19 mm height) coupled to a Hamamatsu (R9779) photomultiplier tube (PMT). The detector has an energy resolution of 6% (@662 keV), and has low internal activity[35]. A 3D-printed sample support was built to ensure the reproducibility of sample positioning. Within 10 min after irradiation, each tumor was excised, weighted, placed in a 0.5-mL microcentrifuge tube and shortly centrifuged. Then, the tube was placed on the detector and the gamma radiation emitted by the sample was recorded for 29 ± 5 min. Afterwards, the tumors were washed with PBS for 5 min with gentle shaking, placed in a new tube, shortly centrifuged and placed back at the detector. In this way, the isotopes in the extracellular matrix and those that can diffuse through cell membranes will be removed leaving mainly those that are entrapped within the cells. Another acquisition was performed for 22 ± 13 min in order to determine the remaining activity entrapped in the tumor after washing. The gamma events recorded by the detector were processed, obtaining decay curves of the events within the 511-keV peak (± 10% energy window width) and subtracting the background obtained from an acquisition with no active sample placed in the detector. The decay curves (A_{meas}) were fitted to a sum of exponentials (see Eq. 1) including the decays of ^{11}C, ^{13}N and ^{18}F (see details in Table 1) in order to obtain the individual contribution for each isotope.

$$A_{meas}(t) = A_{13N}\sum_i exp(-\lambda_{13N}t) + A_{11C}\sum_i exp(-\lambda_{11C}t) + A_{18F}\sum_i exp(-\lambda_{18F}t) \quad (1)$$

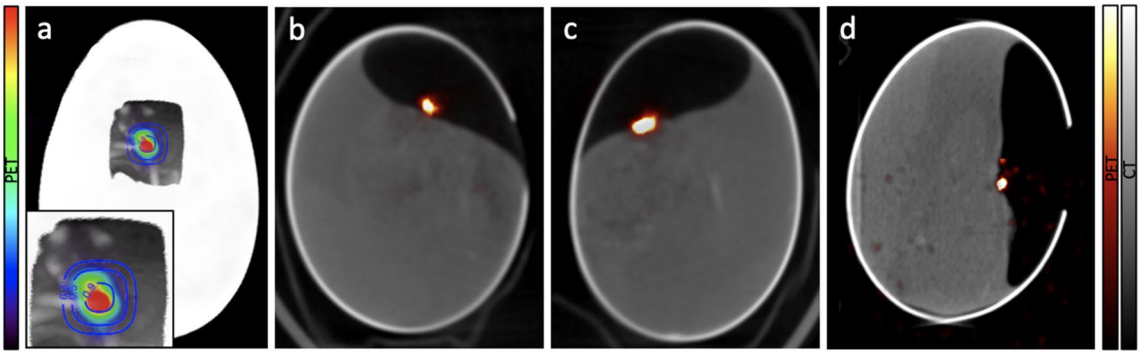

Figure 2. (**a**) Overlay of an estimation of the isodose contours of the delivered dose, the CT and the PET activation for E1. A zoomed image of the irradiated area is shown in the insert. Fused PET and CT images obtained for E1 (**b**), E2 (**c**) and E3 (**d**).

where A_i is the initial activity (fitting parameters) and λ_i is the decay constant for each isotope (i). ^{15}O was not considered as its production cut-off energy (16.79 MeV) is well above the beam energy (8 MeV). The results obtained for each isotope were decay-corrected to the start time of the measurement performed before washing the tumor. In order to reduce the uncertainty of the fit (as the half-lives of ^{13}N and ^{11}C are of the same order of magnitude), a-priori information of the expected activities was employed. Specific activities of each isotope (decay-corrected to the start of the irradiation) can be expressed as:

$$A_{18F} = A_0 N_O f_{18O} \int_0^{E_p} \sigma_{18O(p,n)18F}(E)dE \tag{2}$$

$$A_{13N} = A_0 N_O (1 - f_{18O}) \int_0^{E_p} \sigma_{16O(p,X)13N}(E)dE \tag{3}$$

$$A_{11C} = A_0 N_N \int_0^{E_p} \sigma_{14N(p,X)11C}(E)dE \tag{4}$$

where N_O and N_N are, respectively, the number of oxygen and nitrogen atoms per unit volume, E_p is the incoming proton energy, 7.50 MeV, f_{18O} is the fraction of oxygen atoms of the target substituted by ^{18}O atoms after incubation with 18-W, and A_0 is a constant for each irradiation encapsulating all variables which do not depend on the specific isotope, such as received dose, tumour weight and detector efficiency. From these expressions, the ratio of post-irradiation activities A_{13N}/A_{11C} can be inferred from tissue atomic compositions and reaction cross sections. Assuming an atomic composition of H 9.8%, C 19.5%, N 4.8% and O 65.0% for squamous cell carcinoma[42], and using a Monte Carlo simulation as described in previous works[13], we estimated a ratio $A_{13N}/A_{11C} = (1\text{-}f_{18O}) \cdot 0.394$. The percentage of ^{18}F, ^{11}C and ^{13}N entrapped into the tumor was obtained by comparing their specific activities (decay-corrected to the irradiation time) before and after washing the tumor. Since the activity of ^{13}N was almost negligible after wash (as post-wash measurements were performed over five ^{13}N half-lives after irradiation) we assumed that the activity ratio A_{13N}/A_{11C} was maintained after washout or, in other words, that the washout of generated ^{11}C and ^{13}N was similar. This assumption has negligible impact in determining the maximum retained activity of either ^{11}C or ^{13}N. The percentage of incorporated ^{18}O, or f_{18O}, was calculated by comparing decay-corrected specific activities of ^{18}F and ^{11}C before wash.

Results

In-vivo analysis (PET/CT). The ^{18}F activation was monitored in-vivo on 3 of the irradiated eggs using PET/CT imaging. The chicken embryos remained viable during the entire experiment including irradiation and PET/CT acquisitions. Figure 2A shows an estimation of the dose distribution delivered to E1 overlaid with the CT and the PET activation images. The image is oriented in the beam's eye view. Fused CT and PET images for E1, E2 and E3 are shown on Fig. 2b–d. The PET images for E1 and E2 correspond to the first hour of acquisition and the PET image for E3 corresponds to the entire 10 min acquisition. PET images show a high activity signal on the irradiated tumors placed on the CAM, while only a minor background of diffused activity is observed in the rest of the egg or in the chicken embryo. The opening window in the eggshell can be observed on the CTs of two of the eggs.

The decay curves obtained from the 9-h long dynamic PET images for E1 and E2 are shown on Fig. 3. The curves were fitted to an exponential function corresponding to the physical decay of ^{18}F multiplied by a biological decay function[43]. Combined half lives derived from the fits were (97.6 ± 1.6) min and (101 ± 8) min for E1 and E2, yielding wash-out half lives of (14.7 ± 2.2) and (21 ± 18) h respectively. Therefore, an important result is that the detected activity decays mostly from the disintegration of ^{18}F, i.e., little washout is observed for many hours: the model predicts a biological decrease in ^{18}F activity of less than 32% at 8 h after irradiation.

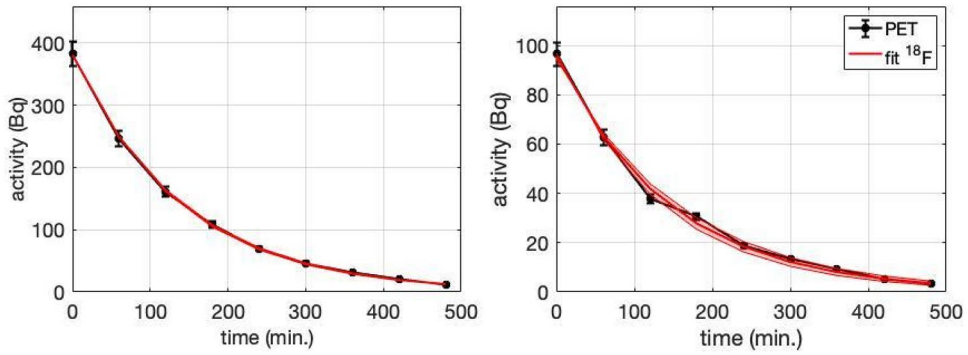

Figure 3. Decay curves of E1 (left) and E2 (right) obtained from dynamic PET images (black) and the fits (red). The red shaded area represents 95% confidence interval of the fit.

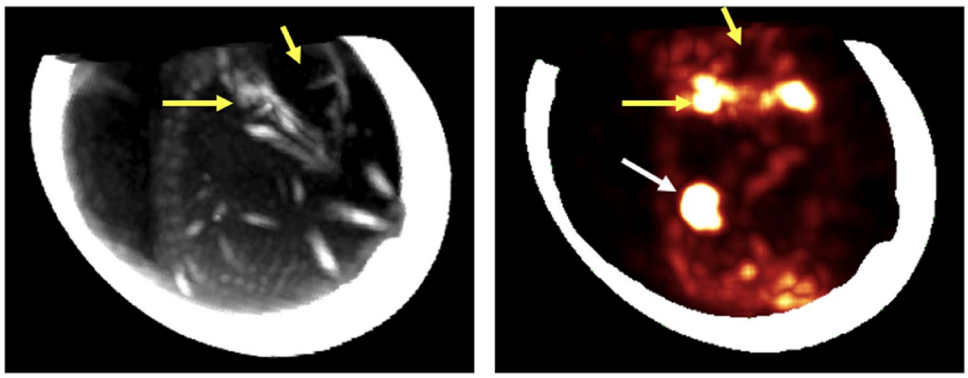

Figure 4. CT (left) and PET (right) maximum intensity projection images of E1. The bony structure of the chicken embryo is observed on the CT and the bone uptake of the produced ^{18}F is observed on the PET image (yellow arrows show the jaw joint with high uptake and the cranial cavity with no uptake) as well as the activity produced in the tumor (white arrow). PET image is overlaid with the eggshell. PET and CT images could not be overlaid due to motion of the chicken embryo.

From this result, we can infer that the produced ^{18}F ions remain largely entrapped within the tumor cells, held by the electronegative potential of the cell membrane.

Figure 4 displays another activity map (with increased contrast) showing some ^{18}F activity away from the target area. This activity corresponds to 18-W present in the extracellular space (or blood vessels) at the time of irradiation. This ^{18}F is created outside the cell membrane and reaches other areas of the chicken embryo through diffusion or circulation. Moreover, some of this radioactive fluorine appears to cluster in the bony structures of the chicken embryo. Indeed, ^{18}F-NaF is a well-known radiotracer used to monitor osteogenic activity for the detection of osseous metastases[38].

Ex-vivo analysis ($CeBr_3$ detector). The tumors from 4 of the irradiated eggs (T1–T4) were excised after the irradiation and analysed with the $CeBr_3$ detector before and after washing the tumor with PBS. Figure 5 shows the decay curves measured with the gamma detector for the irradiated eggs and the fits obtained with the contribution of different isotopes. Results are shown for measurements performed before and after washing the tumor with PBS. A large production of ^{18}F can be observed before washing the tumor with contributions from ^{11}C and ^{13}N.

Figure 6 (top) shows absolute specific activity of the three considered isotopes at the beginning of each measurement, obtained from the fits. Differences in activity between T1–T4 tumours can be explained by tumour size, ^{18}O captation, and time elapsed between irradiation and start of measurement. Estimated captation levels (in unwashed tumors) ranged from a minimum of 0.61% in T1 to a maximum of 3.0% in T4, expressed as the fraction of ^{16}O atoms replaced by ^{18}O, or f_{18O}.

Figure 6 (bottom) shows the percentage of retained activity of the different isotopes considered, calculated as the ratio of activities corrected by the physical decay, analyzed ex-vivo with the gamma detector. The weighted average shows a retention of (59 ± 9)% for ^{18}F, significantly higher than the estimated retention of ^{11}C and ^{13}N, calculated at (14 ± 26)%. The high uncertainty in this number is due to the shorter half-lives of ^{11}C and ^{13}N, as most of their activity had physically decayed by the time the post-wash measurements were performed. Still, the results for the washed tumors highlight that a large portion of the produced ^{18}F remains entrapped in the tumor while all other isotopes have been washed out or have physically decayed.

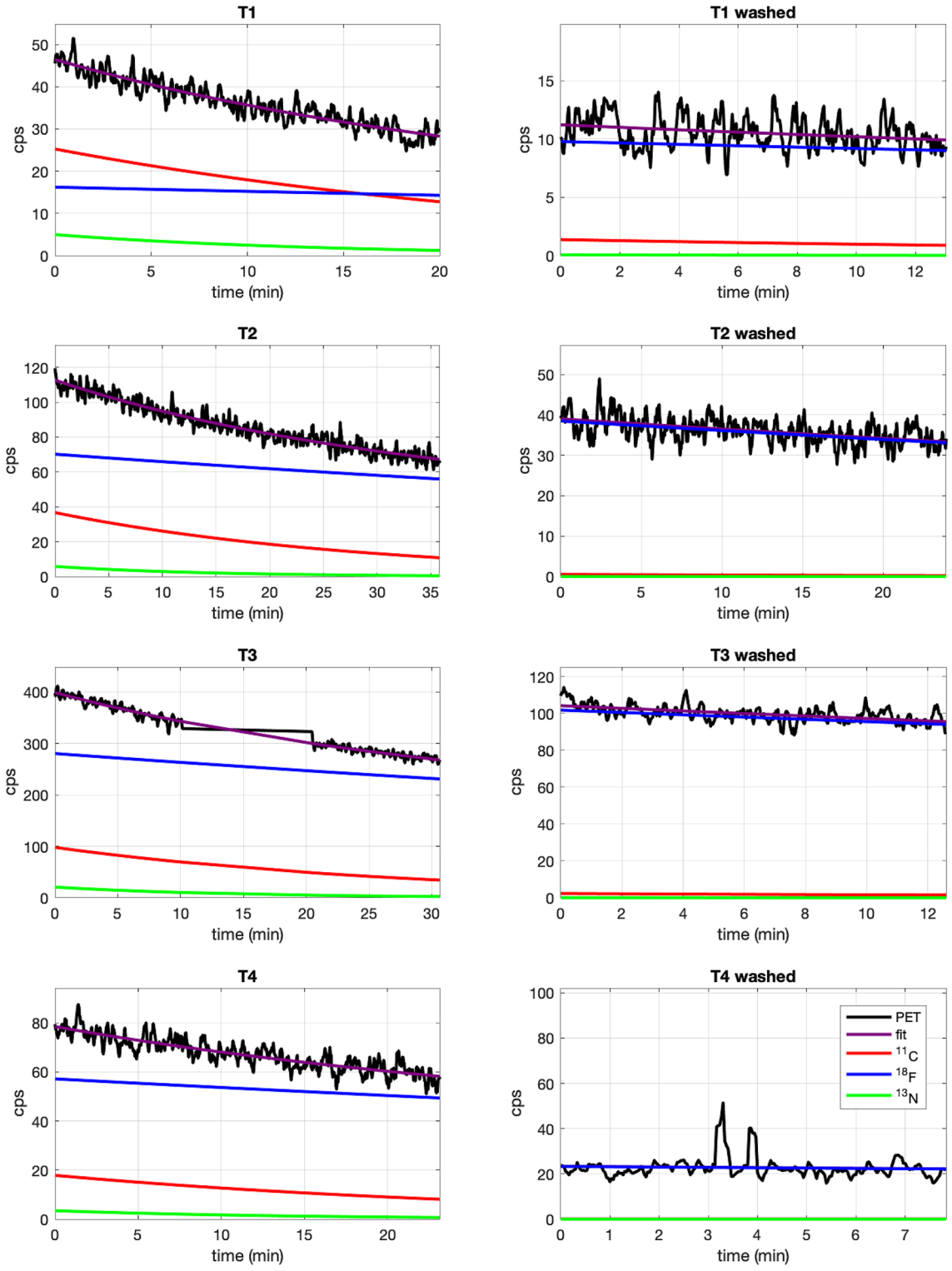

Figure 5. Decay curves (black) of gamma events recorded with the $CeBr_3$ detector from tumors T1–T4 inoculated with 18-W and irradiated with a proton beam before (left) and after (right) washing the tumor with PBS. Decay curves were fitted (purple) to a sum of exponentials to obtain the contribution from ^{11}C (red), ^{13}N (green) and ^{18}F (blue). Measurement of T3 activity was stopped for 10 min and then resumed, hence the gap in activity shown in the plot.

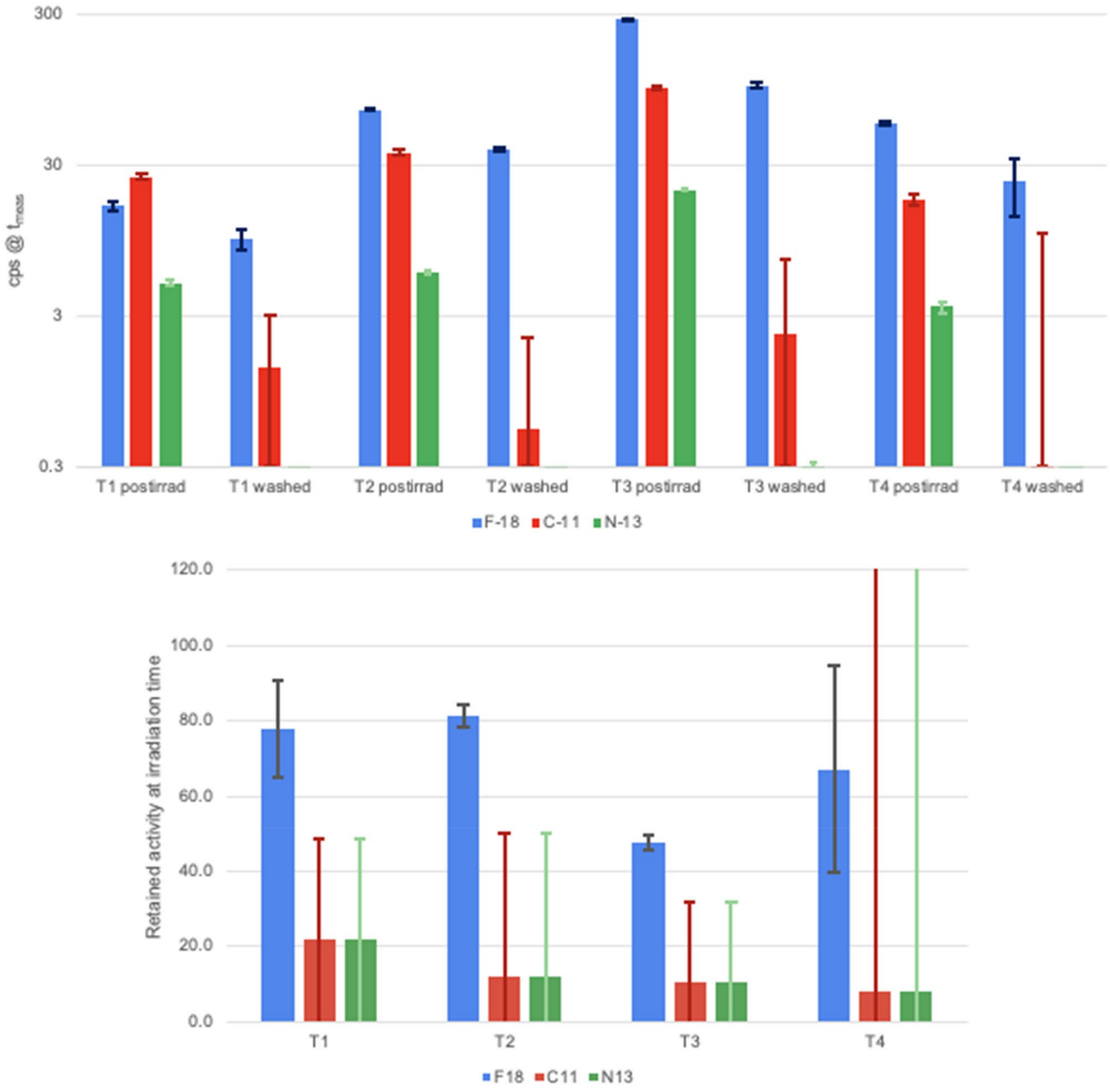

Figure 6. (top) Measured activity in counts per second (cps) from tumors T1–T4 corresponding to ^{11}C (red), ^{13}N (green), and ^{18}F (blue) at the beginning of the measurements (t_{meas}), performed at post-irradiation time and on washed tumors. (bottom) Percentage of retained activity on the irradiated tumors (T1–T4) obtained by comparison of the decay-corrected specific activity at the irradiation time before and after washing the tumors. Error bars represent the 1-sigma confidence interval.

Discussion

Analysis of the observed results. In this study, the proton activation in the last millimeter of the proton path was observed in-vivo by PET imaging. For this purpose, we inoculated 18-W into the tumor of a chicken embryo CAM tumor model of head and neck cancer prior to proton irradiation inducing the production of ^{18}F that gets entrapped inside the tumor and can be later detected by PET imaging. Furthermore, we observed for the first time the biodistribution of in-vivo produced ^{18}F radiotracer in the bony structures of the chicken embryo (see Fig. 4).

The use of 18-W for proton range verification was first proposed by Cho et al.[21–23] using implantable markers or hydrogels encapsulating 18-W and its feasibility was tested in phantoms. Instead, we proposed in a previous study the direct administration of 18-W to the patient[13]. In the present work we test this approach in an animal model for the first time. Several range verification techniques have already been tested in patients[3,4,6] although they are still not used in the clinical routine.

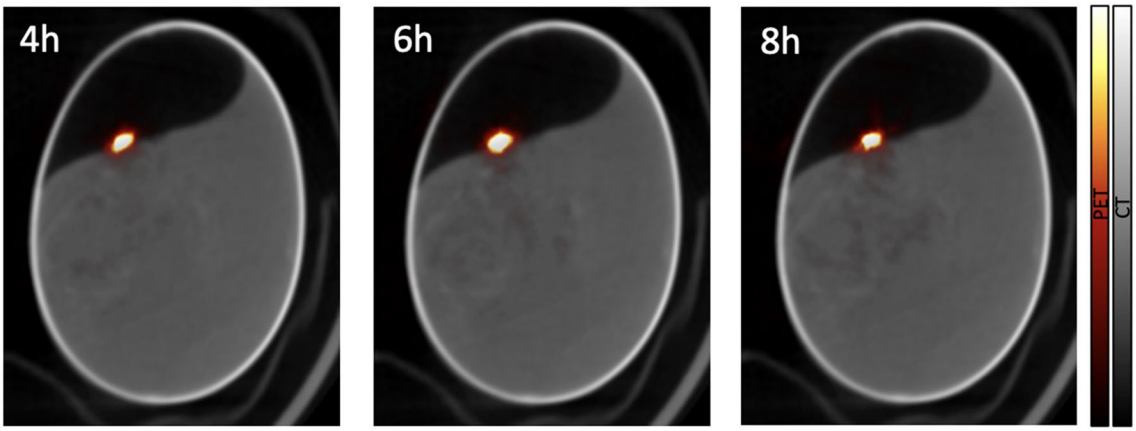

Figure 7. Fused PET and CT images obtained for E1 acquired 4 (left), 6 (middle), and 8 (right) hours after irradiation. The color scale of the PET images was adjusted for each particular image.

The low energy threshold in the production of ^{18}F (2.6 MeV, proton range in water of 115 μm) induces sample activation in very close proximity to the end of the proton path, enabling more accurate range verification than other isotopes, such as ^{11}C and ^{15}O, which are not produced in the last few mm. The 8-MeV proton beam was used to irradiate the implanted tumor onto the CAM, previously inoculated with 18-W. This led to 7.5-MeV protons entering the tumor with a range in water of 740 μm, ensuring that dose deposition and activation occurred only at the equivalent of the distal end of a clinical beam. Results shown in Fig. 6 demonstrate that most of the remaining activity in the tumor a few minutes after irradiation corresponds to ^{18}F and more than half of the produced ^{18}F is entrapped within the tumor. Long-term entrapment of ^{18}F was confirmed in-vivo by the dynamic PET images obtained for two of the irradiated eggs (E1 and E2).

Determination of retained activity was measured with reasonable accuracy (better than 10%) for ^{18}F, but with not so good accuracy for ^{11}C and ^{13}N, due to the long time elapsed between irradiation and post-wash measurements. However, available data allows us to calculate an upper limit on the activity retention for ^{11}C and ^{13}N at 40%, proving that ^{18}F is retained in the cells at a significantly higher quantity than other produced isotopes. Still, further studies with shorter delay times between pre-wash and post-wash measurements would be required to increase the accuracy of the entrapment measurements for short-lived isotopes.

The mechanism for the entrapment of ^{18}F within the tumor may be explained as follows. Water is a diffusible agent that is not extracted or entrapped within the cells but rather freely diffuses across membranes[45]. Once the ^{18}F ion is produced, it no longer has the ability to cross the cell membrane due to its charge, and gets intracellularly entrapped if produced within the cytoplasm[46]. Although the anionic channels in the cells are not highly specific, it is known that they show only a very small permeability to the fluoride ion[47]. In addition, ^{18}F in aqueous solution forms hydrogen bonds with the surrounding water molecules and becomes unreactive for nucleophilic substitution[48].

Remaining challenges for clinical application. In order to produce enough ^{18}F activity allowing for its visualization using PET scanners, a high concentration of 18-W within the tumor is required. In this study, the 18-W buffer was directly applied on top of the tumor as is typically performed for drug administration in the chicken CAM model. For clinical application, different routes of administration and irradiation protocols must be explored to ensure maximal concentration of 18-W in the tumor and surrounding tissues, while using a reasonable amount of this costly contrast agent. ^{18}O-water is regularly used all around the world as a target for production of ^{18}F for PET imaging. In addition, doubly labeled water ($^{2}H_{2}{}^{18}O$) has been used for decades for measuring energy expenditure in free-living animals[49] and in humans[50]. In any case, we must explore techniques that allow obtaining and using ^{18}O-water at a reduced cost. The dose delivered to the tumor in this study was noticeably higher than in a typical clinical fraction (~ 2 Gy) and the sensitivity of the preclinical PET scanner is about 5 times higher than that of a clinical PET scanner. In this work, usable PET images were still obtained from 4 to 8 h after irradiation (where initial activity had decayed by factors of 4.5 and 20, respectively, as displayed in Fig. 7) and E3 was irradiated with a much lower dose than E1 and E2 and the activation was clearly visible one hour after irradiation (see Fig. 2D).

In order to estimate the clinical feasibility of the proposed technique, we performed a Monte Carlo simulation using TOPAS[51]. A proton beam of 8 MeV was used to deliver a dose of 2 Gy at the Bragg Peak to a target containing 30% of 18-W achieving a ^{18}F activity of 0.5 Bq/mm^3. A minimum detectable activity of 148 Bq/mm^3 has been reported for clinical PET scanners[52]. However, the latest generation of PET scanners[53,54] provide many technological improvements including increased sensitivity, excellent time-of-flight resolution and advanced reconstruction algorithms which may allow for the detection of lower activity concentration. Furthermore, those estimations were made for standard clinical scan duration (3–5 min) and signal to background ratio while PET scans for proton range verification can be extended for 20–30 min in a single bed position and there is no activity out of the irradiated volume. Finally, there is ample room for improvement in ^{18}O captation (estimated at below 3% for this study), suggesting that lower doses could be explored if captation is increased. Therefore,

future experiments should evaluate the feasibility of the proposed technique in an environment closer to the clinical conditions.

In a previous phantom study[13], we have shown that the position of the Bragg peak can be determined within 2 mm when having 10% 18-W after a 20 Gy proton beam irradiation. Therefore, we can expect that all previously mentioned improvements could provide a similar range verification accuracy in an in-vivo setup.

As mentioned in the introduction, proton range verification can also be performed using in-beam PET detectors[16] and very-short-lived isotopes[17]. Those techniques would benefit from some of the improvements mentioned above, like increased sensitivity and improved time-of-flight resolutions. Therefore, future studies will be needed to determine which technique suits better for clinical application. In addition, range verification based on prompt gamma imaging has been recently tested in a clinical environment showing promising results, although further studies are required, particularly for beams with high instantaneous currents[39,55].

Conclusion

The use of 18-W as a suitable contrast agent for in-vivo range verification in proton therapy has been evaluated in-vivo in a chicken embryo CAM tumor model of head and neck cancer. Results show ^{18}F activation and retention within the tumor in the last millimeter of the proton range, which enables direct proton range measurement using offline PET imaging. The longer half-life of ^{18}F makes it possible to detect it in readily available PET scanners more than 2 h after irradiation to minimize the contribution from other isotopes with high production thresholds while a large fraction of the produced ^{18}F remains entrapped within the tumor cells.

The observed results encourage us to proceed with further in-vivo experiments in larger animals and with clinically relevant proton beam energies to validate and assess the capabilities of 18-W as a suitable contrast agent for range verification in proton therapy. In order to achieve a high-enough ^{18}O concentration in the irradiated volume, different routes of administration and irradiation protocols will also be studied.

Received: 27 April 2021; Accepted: 18 April 2022
Published online: 30 April 2022

References

1. Jermann, M. PTCOG Patient Statistics. http://ptcog.web.psi.ch/ (2020).
2. Paganetti, H. Range uncertainties in proton therapy and the role of Monte Carlo simulations. *Phys. Med. Biol.* **57**(11), R99–R117. https://doi.org/10.1088/0031-9155/57/11/R99 (2012).
3. Parodi, K. *et al.* Patient study of in vivo verification of beam delivery and range, using positron emission tomography and computed tomography imaging after proton therapy. *Int. J. Radiat. Oncol. Biol. Phys.* **68**, 920–934. https://doi.org/10.1016/j.ijrobp.2007.01.063 (2007).
4. Zhu, X. *et al.* Monitoring proton radiation therapy with in-room PET imaging. *Phys. Med. Biol.* **56**(13), 4041–4057. https://doi.org/10.1088/0031-9155/56/13/019 (2011).
5. Min, C. H. *et al.* Prompt gamma measurements for locating the dose fall-off region in the proton therapy. *Appl. Phys. Lett.* **89**, 183517 (2006).
6. Richter, C. *et al.* First clinical application of a prompt gamma based in vivo proton range verification system. *Radiother. Oncol.* **118**(2), 232–237 (2016).
7. Assmann, W. *et al.* Ionoacoustic characterization of the proton Bragg peak with submillimeter accuracy. *Med. Phys.* **42**(2), 567–574 (2015).
8. Gensheimer, M. F. *et al.* In vivo proton beam range verification using spine MRI changes. *Int. J. Radiat. Oncol. Biol. Phys.* **78**, 268–275 (2010).
9. Knopf, A. C. & Lomax, A. In vivo proton range verification: A review. *Phys. Med. Biol.* **58**(15), R131–R160 (2013).
10. España, S. *et al.* The reliability of proton-nuclear interaction cross-section data to predict proton-induced PET images in proton therapy. *Phys. Med. Biol.* **56**(9), 2687–2698. https://doi.org/10.1088/0031-9155/56/9/003 (2011).
11. Litzenberg, D. W. *et al.* On-line monitoring of radiotherapy beams: Experimental results with proton beams. *Med. Phys.* **26**, 992–1006. https://doi.org/10.1118/1.598491 (1999).
12. Cho, J. *et al.* Feasibility study of using fall-off gradients of early and late PET scans for proton range verification. *Med. Phys.* **44**(5), 1734–1746 (2017).
13. España, S. *et al.* Direct proton range verification using oxygen-18 enriched water as a contrast agent. *Radiat. Phys. Chem.* **182**, 9385 (2021).
14. Parodi, K., Ponisch, F. & Enghardt, W. Experimental study on the feasibility of in-beam PET for accurate monitoring of proton therapy. *IEEE Trans Nucl. Sci.* **52**, 778. https://doi.org/10.1109/NSSMIC.2004.1462690 (2005).
15. Ferrero, V. *et al.* Online proton therapy monitoring: Clinical test of a Silicon-photodetector-based in-beam PET. *Sci. Rep.* **8**(1), 1–8. https://doi.org/10.1038/s41598-018-22325-6 (2018).
16. Surti, S. *et al.* Design study of an in situ PET scanner for use in proton beam therapy. *Phys. Med. Biol.* **56**, 2667–2685. https://doi.org/10.1088/0031-9155/56/9/002 (2011).
17. Ozoemelam, I. *et al.* Feasibility of quasi-prompt PET-based range verification in proton therapy. *Phys. Med. Biol.* **65**(24). https://doi.org/10.1088/1361-6560/aba504 (2020).
18. Ozoemelam, I. *et al.* Real-time PET imaging for range verification of helium radiotherapy. *Front. Phys.* **8**(October), 1–16. https://doi.org/10.3389/fphy.2020.565422 (2020).
19. Rodriguez, A. *et al.* Can iodine be used as a contrast agent for protontherapy range verification? Measurement of the 127I (p, n) 127mXe (reaction) cross section in the 4.5–10 MeV energy range. *Radiat. Phys. Chem.* **185**, 109485. https://doi.org/10.1016/j.radphyschem.2021.109485 (2021).
20. Fraile, L. M. *et al.* Experimental validation of gallium production and isotope-dependent positron range correction in PET. *Nucl. Instrum. Meth. A.* **814**. https://doi.org/10.1016/j.nima.2016.01.013 (2016).
21. Cho, J. *et al.* Feasibility of hydrogel fiducial markers for in vivo proton range verification using PET. *Phys. Med. Biol.* **61**(5), 2162–2176. https://doi.org/10.1088/0031-9155/61/5/2162 (2016).
22. Cho, J. *et al.* Feasibility of proton-activated implantable markers for proton range verification using PET. *Phys. Med. Biol.* **58**, 7497–7512. https://doi.org/10.1088/0031-9155/58/21/7497 (2013).
23. Cho, J. *et al.* Characterizing proton-activated materials to develop PET-mediated proton range verification markers. *Phys. Med. Biol.* **61**(11), N291–N310. https://doi.org/10.1088/0031-9155/61/11/N291 (2016).

24. Speakman, J. R. The history and theory of the doubly labeled water technique. *Am. J. Clin. Nutr.* **68**, 932–938. https://doi.org/10.1093/ajcn/68.4.932S (1998).
25. Toramatsu, C. *et al.* Biological washout modelling for in-beam PET: Rabbit brain irradiation by 11C and 15O ion beams. *Phys. Med. Biol.* **65**(10), 105011. https://doi.org/10.1088/1361-6560/ab8532 (2020).
26. Nowak-Sliwinska, P., Segura, T. & Iruela-Arispe, M. L. The chicken chorioallantoic membrane model in biology, medicine and bioengineering. *Angiogenesis* **17**(4), 779–804. https://doi.org/10.1007/s10456-014-9440-7 (2014).
27. Schwartz, D. L. & Hayes, D. N. The evolving role of radiotherapy for head and neck cancer. *Hematol. Oncol. Clin. North Am.* **34**(1), 91–108. https://doi.org/10.1016/j.hoc.2019.08.019 (2020).
28. Blanchard, P. *et al.* Proton therapy for head and neck cancers. *Semin. Radiat. Oncol.* **28**(1), 53–63. https://doi.org/10.1016/j.semradonc.2017.08.004 (2018).
29. Bragado, P. *et al.* Analysis of marker-defined HNSCC subpopulations reveals a dynamic regulation of tumor initiating properties. *PLoS ONE* **7**(1), e29974. https://doi.org/10.1371/journal.pone.0029974 (2012).
30. Bragado, P. *et al.* TGF-β2 dictates disseminated tumour cell fate in target organs through TGF-β-RIII and p38α/β signalling. *Nat. Cell Biol.* **15**(11), 1351–1361. https://doi.org/10.1038/ncb2861 (2013).
31. Toolan, H. W. Transplantable human neoplasms maintained in cortisone-treated laboratory animals: H.S. No. 1; H.Ep. No. 1; H.Ep. No. 2; H.Ep. No. 3; and H.Emb.Rh. No. 1. *Cancer Res.* **14**(9), 660–666. (1954).
32. Ossowski, L., Russo, H., Gartner, M. & Wilson, E. L. Growth of a human carcinoma (HEp3) in nude mice: Rapid and efficient metastasis. *J. Cell Physiol.* **133**(2), 288–296. https://doi.org/10.1002/jcp.1041330212 (1987).
33. Aguirre Ghiso, J. A., Kovalski, K. & Ossowski, L. Tumor dormancy induced by downregulation of urokinase receptors in human carcinoma involves integrin and MAPK signaling. *J. Cell Biol.* **147**(1), 89–104. https://doi.org/10.1083/jcb.147.1.89 (1999).
34. Enguita, O. *et al.* The new external microbeam facility at the 5 MV Tandetron accelerator laboratory in Madrid: Beam characterisation and first results. *Nucl. Instrum. Methods Phys. Res., Sect. B* **219**, 384–388. https://doi.org/10.1016/j.nimb.2004.01.087 (2004).
35. Sánchez-Parcerisa, D. *et al.* Integrated positioning and treatment planning system for irradiation of biological samples with low-energy protons (in preparation).
36. Berger, M. J., Coursey, J. S., & Zucker, M. A. *ESTAR, PSTAR, and ASTAR: computer programs for calculating stopping-power and range tables for electrons, protons, and helium ions* (version 1.21) (No. http://physics.nist.gov/Star) (1999).
37. Sánchez-Parcerisa, D., Kondrla, M., Shaindlin, A. & Carabe, A. FoCa: A modular treatment planning system for proton radiotherapy with research and educational purposes. *Phys. Med. Biol.* **59**(23), 7341–7360. https://doi.org/10.1088/0031-9155/59/23/7341 (2014).
38. Sanchez-Parcerisa, D. *et al.* Radiochromic film dosimetry for protons up to 10 MeV with EBT2, EBT3 and unlaminated EBT3 films. *Phys. Med. Biol.* **66**(11), 115006 (2021).
39. López-Montes, A. *et al.* IEEE nuclear science symposium and medical imaging conference (NSS/MIC). *Manchester, United Kingdom* **2019**, 1–3. https://doi.org/10.1109/NSS/MIC42101.2019.9059837 (2019).
40. Herraiz, J. L., España, S., Vaquero, J. J., Desco, M. & Udías, J. M. FIRST: Fast iterative reconstruction software for (PET) tomography. *Phys. Med. Biol.* **51**, 4547–4565. https://doi.org/10.1088/0031-9155/51/18/007 (2006).
41. Fraile, L. M. *et al.* Fast timing study of a CeBr 3 crystal: Time resolution below 120 ps at 60Co energies. *Nucl. Instrum. Methods Phys. Res. A.* **701**, 235–242 (2013).
42. Maughan, R. L., Chuba, P. J., Porter, A. T., Ben-Josef, E. & Lucas, D. R. The elemental composition of tumors: Kerma data for neutrons. *Med. Phys.* **24**(8), 1241–1244 (1997).
43. Tomitani, T. *et al.* Washout studies of 11C in rabbit thigh muscle implanted by secondary beams of HIMAC. *Phys. Med. Biol.* **48**(7), 875 (2003).
44. Araz, M., Aras, G. & Küçük, Ö. N. The role of 18F-NaF PET/CT in metastatic bone disease. *J. Bone Oncol.* **4**(3), 92–97. https://doi.org/10.1016/j.jbo.2015.08.002 (2015).
45. Ho, V., & Reddy G. *Cardiovascular Imaging*. ISBN: 9780323246910 eBook ISBN: 9781455706976. Saunders (2010).
46. Lodish, H. *et al. Molecular cell biology* 4th edn. (W. H. Freeman, 2000).
47. Simchowitz, L. Interactions of bromide, iodide, and fluoride with the pathways of chloride transport and diffusion in human neutrophils. *J. Gen. Physiol.* **91**(6), 835–860 (1988).
48. Jacobson, O., Kiesewetter, D. O. & Chen, X. Fluorine-18 radiochemistry, labeling strategies and synthetic routes. *Bioconjug. Chem.* **26**(1), 1–18 (2015).
49. Lifson, N., Gordon, G. B. & McClintock, R. Measurement of total carbon dioxide production by means of D2O18. *J. Appl. Physiol.* **7**(6), 704–710 (1955).
50. Schoeller, D. A. & van Santen, E. Measurement of energy expenditure in humans by doubly labeled water method. *J. Appl. Physiol. Respir. Environ. Exerc. Physiol.* **53**(4), 955–959 (1982).
51. Perl, J., Shin, J., Schumann, J., Faddegon, B. & Paganetti, H. TOPAS: An innovative proton Monte Carlo platform for research and clinical applications. *Med. Phys.* **39**(11), 6818–6837 (2012).
52. Karakatsanis, N.A., & Nikita, K.S. A study of the parameters affecting minimum detectable activity concentration level of clinical LSO PET scanners in *2008 8th IEEE International Conference on BioInformatics and BioEngineering, Athens*, Greece, pp. 1–6 (2008).
53. Rausch, I. *et al.* Performance evaluation of the Philips Vereos PET/CT system according to the NEMA NU2–2012 standard. *J. Nucl. Med.* **43**, 1 (2018).
54. van Sluis, J. *et al.* Performance characteristics of the digital biograph vision PET/CT system. *J. Nucl. Med.* **60**(7), 1031–1036 (2019).
55. Hueso-González, F. A full-scale clinical prototype for proton range verification using prompt gamma-ray spectroscopy. *Phys. Med. Biol.* **63**, 5019. https://doi.org/10.1088/1361-6560/aad513 (2018).

Acknowledgements

This work was funded by Comunidad de Madrid under project B2017/BMD-3888 PRONTO-CM "Proton-therapy and nuclear techniques for oncology." Support by the Spanish Government (MCIU/AEI, FEDER, EU) via projects RTI2018-098868-B-I00, RTC-2015-3772-1, SAF2016-76588-C2-1-R, RTC-2019-007112-1, by European Regional Funds and the European Union's Horizon 2020 research and innovation programme under the Marie Sklodowska-Curie grant agreement No 793576 (CAPPERAM) and by BBVA (becas Leonardo 2018, BBM-TRA-0041) is acknowledged. This is a contribution for the Moncloa Campus of International Excellence, "Grupo de Física Nuclear-UCM", Ref. 910059. Part of the calculations of this work were performed in the "Clúster de Cálculo para Técnicas Físicas", funded in part by UCM and in part by EU Regional Funds. S. España is supported by the Comunidad de Madrid (2016-T1/TIC-1099) and A. Gutierrez-Uzquiza is supported by the Comunidad de Madrid (2017-T1/BMD-5468). The CNIC is supported by the Instituto de Salud Carlos III (ISCIII); the Ministerio de Ciencia, Innovación y Universidades (MCNU); and the Pro CNIC Foundation, and is a Severo Ochoa Center of Excellence (SEV-2015-0505). The authors acknowledge the support of SEDECAL staff to perform the PET and CT images in their facilities and the CMAM technical staff for their assistance during the experiments.

Author contributions

S.E., D.S.P., P.B., A.G.U., J.M.U and L.M.F. designed the experiments. S.E., D.S.P., P.B., A.G.U., A.E., C.G.N., V.V.O., P.I., V.S.T, J.M.U and L.M.F. carried out the experiments. S.E., D.S.P., J.M.U, A.E., V.V.O. and V.S.T analyzed the data. S.E., D.S.P, J.M.U, and L.M.F. wrote the manuscript. All authors read, provided feedback and approved the manuscript.

Funding

This article was funded by Comunidad de Madrid (B2017/BMD-3888, 2017-T1/BMD-5468), European Union (793576), Spanish Government (SAF2016-76588-C2-1-R, RTI2018-098868-B-I00, RTI2018-098868-B-I00, BBVA, BBM-TRA-0041, BBM-TRA-0041).

Competing interests

The authors declare no competing interests.

Additional information

Correspondence and requests for materials should be addressed to S.E.

Reprints and permissions information is available at www.nature.com/reprints.

Publisher's note Springer Nature remains neutral with regard to jurisdictional claims in published maps and institutional affiliations.